catalysts

MDPI

Article

V_2O_5/Carbon Nanotube/Polypyrrole Based Freestanding Negative Electrodes for High-Performance Supercapacitors

Jincy Parayangattil Jyothibasu [1], Ming-Zhu Chen [1], You-Ching Tien [1], Chi-Ching Kuo [2], Erh-Chiang Chen [3], Yi-Chun Lin [3], Tai-Chin Chiang [4] and Rong-Ho Lee [1,*]

1 Department of Chemical Engineering, National Chung Hsing University, Taichung 402, Taiwan; jincycusat@gmail.com (J.P.J.); aabb879546aabb48@gmail.com (M.-Z.C.); poweramoney@googlemail.com (Y.-C.T.)
2 Research and Development Center of Smart Textile Technology, Institute of Organic and Polymeric Materials, National Taipei University of Technology, Taipei 10608, Taiwan; kuocc@mail.ntut.edu.tw
3 Instrument Center, National Chung Hsing University, Taichung 402, Taiwan; erhchiang.chen@gmail.com (E.-C.C.); chchlin@dragon.nchu.edu.tw (Y.-C.L.)
4 Global Development Engineering Program, National Taiwan University of Science and Technology, Taipei 10607, Taiwan; tcchiang0102@gmail.com
* Correspondence: rhl@nchu.edu.tw; Tel.: +886-4-22854308; Fax: +886-4-22854734

Abstract: In this study, the vanadium pentoxide (V_2O_5), functionalized carbon nanotubes (*f*-CNT), and polypyrrole (PPy) based composites films have been prepared through a facile synthesis method and their electrochemical performance were evaluated as freestanding negative electrodes of supercapacitor. A hydrous V_2O_5 gel prepared by treating V_2O_5 powder with H_2O_2 was mixed with *f*-CNT to obtain V_2O_5/*f*-CNT composite film. V_2O_5/*f*-CNT composite was then coated with PPy through vapor phase polymerization method. The PPy deposited on the V_2O_5/*f*-CNT prevented the dissolution of V_2O_5 and thus resulted in an improved the capacitance and cycle life stability for V_2O_5/*f*-CNT/PPy composite electrode. V_2O_5/*f*-CNT/PPy freestanding negative electrode exhibited a high areal capacitance value (1266 mF cm^{-2} at a current density of 1 mA cm^{-2}) and good cycling stability (83.0% capacitance retention after 10,000 charge-discharge cycles). The superior performance of the V_2O_5/*f*-CNT/PPy composite electrode can be attributed to the synergy between *f*-CNT with high conductivity and V_2O_5 and PPy with high-energy densities. Thus, V_2O_5/*f*-CNT/PPy composite based electrode can effectively mitigate the drawbacks of the low specific capacitance of CNTs and the poor cycling life of V_2O_5.

Keywords: carbon nanotube; freestanding negative electrode; polypyrrole; vanadium pentoxide gel; supercapacitor

check for updates

Citation: Jyothibasu, J.P.; Chen, M.-Z.; Tien, Y.-C.; Kuo, C.-C.; Chen, E.-C.; Lin, Y.-C.; Chiang, T.-C.; Lee, R.-H. V_2O_5/Carbon Nanotube/Polypyrrole Based Freestanding Negative Electrodes for High-Performance Supercapacitors. *Catalysts* **2021**, *11*, 980. https://doi.org/10.3390/catal11080980

Academic Editor: Enrique García-Bordejé

Received: 24 July 2021
Accepted: 14 August 2021
Published: 16 August 2021

1. Introduction

Electrochemical supercapacitors (SCs) have recently attracted a lot of attention due to their high power density, fast charging/discharging rates, high cycling stability, low fabrication costs, and environmental friendliness, making them a good candidate for use as the energy storage system for hand-held portable devices, wearable electro-optical devices, and sensors [1,2]. According to the energy storage mechanism, SCs can be divided into electrical double-layer capacitors (EDLCs) and pseudocapacitors [3–6]. The carbon materials based EDLCs store energy by the formation of the electrical double layer via electrostatic attraction at the electrode/electrolyte interface, which exhibits fast charging/discharging kinetics, wide potential window, high power density, and high cycling stability, but EDLC is limited by their low specific capacitance [3,7]. The conducting polymer, transition metal compounds, and redox-active materials-based pseudocapacitors store energy by the fast and reversible redox reaction at the electrode/electrolyte interface [8]. Although the pseudocapacitors have a high capacitance behavior, they have limited cycle stability and rate

capability [9–13]. In order to improve the energy storage properties, the hybrid SCs fabricated from the electrode consisting of carbon materials, conducting polymer, transition metal compound, and redox-active material have been developed [14–17].

Transition-metal oxides (TMOs), such as ruthenium oxide (RuO_2), manganese dioxide (MnO_2), vanadium pentoxide (V_2O_5), iron oxide (Fe_2O_3), and Co_3O_4, have been explored for use in pseudocapacitors [18–21]. TMOs based SCs exhibited better electrochemical stability than the conducting polymer and higher specific capacitance than conventional carbon materials [22]. Among the TMOs, RuO_2 is one of the promising performers among the electrode materials, but high cost, scarcity, and toxicity hinder its extensive usage [23]. In contrast, V_2O_5 is inexpensive, which has been studied as cathode materials for SCs, due to its high theoretical capacitance (2020 F g^{-1}), large voltage window (up to −2.8 V), low cost, and abundance [24,25]. The balanced oxidation states and layered structures with a large surface area of V_2O_5 allow a much higher charge storage capacity than other cheap TMOs [26–28]. Since V_2O_5 exhibits a low electrical conductivity and cycling instability, V_2O_5/active carbon fabric (ACF), V_2O_5/CNT, and V_2O_5/graphene oxide (GO) nanocomposites have been developed to improve electrode performance for SCs [29–38]. The 3D array of layered V_2O_5 grown on activated carbon fabric (ACF) for SC has been reported by Panigrahi et al. [29]. The 3D network with the porous structure on the ACF can significantly maximize the active material's performance, making it a potential contender in the modern flexible electronics arena. Moreover, the supercapactance of the functionalized CNTs coated with a thin layer of V_2O_5 has been reported by Sathiya et al. [39]. The V_2O_5/CNT composite exhibits both high power density and high energy density, stressing the benefits of using carbon substrates to design high-performance supercapacitor electrodes. In addition, Pande et al. report a simple chemical bath deposition method for the preparation of the V_2O_5/CNT composite with nanoscale architecture [40]. The V_2O_5/CNT with unique nanostructured morphology exhibits the larger electrochemical potential window, which favors greater electrochemical features for SC. High-performance supercapacitors based on intertwined CNT/V_2O_5 nanowire nanocomposites have been reported by Chen et al. [41]. The intertwined CNT/V_2O_5 nanocomposite electrode exhibits excellent rate capability, high capacity, and cycling stability. On the other hand, free-standing three-dimensional V_2O_5 nanobelts coated with conducting poly(3,4-ethylenedioxythiophene) (PEDOT) on vertically aligned CNTs (VA-CNTs)/graphene foam (GF) for flexible energy storage devices has been reported by Jiang et al. [42]. The well-aligned structure of VA-CNTs, and light-weight, highly conductive GF leads to highly efficient ionic and electronic transport channels, which are of scientific and practical significance for energy storage/conversion applications.

In this study, a hydrous V_2O_5 gel prepared by treating V_2O_5 powder with H_2O_2 was mixed with *f*-CNT to obtain V_2O_5/*f*-CNT composite. In order to improve the conductivity and electrochemical properties of the V_2O_5/CNTs composites, the conducting polymer PPy was deposited on the surface of V_2O_5/*f*-CNT electrode by the vapor phase polymerization of pyrrole. The deposition of PPy by vapor phase polymerization favors for the uniform coating of PPy polymer chains on the surface of V_2O_5/*f*-CNT composite. The presence of conducting polymers, such as PPy, polyaniline, and PEDOT have been proven to improve the electrical conductivity of V_2O_5 [43–45]. Bi et al. have reported that the oxygen vacancies could be induced on the surface of V_2O_5 during the oxidative polymerization of the conducting polymer [46,47]. The induced oxygen vacancies promote the charge transfer kinetics of the resulting oxygen vacancies-V_2O_5/conducting polymer nanocables by forming a local electric field. The accompanying $V4^+$ and $V3^+$ may also catalyze the redox reactions and improve the supercapacitor performance [48]. Here, we have investigated the effect of the pyrrole deposition on the morphology, surface area, and electrochemical properties of the resulting V_2O_5/*f*-CNT/PPy composite. The chemical structure of the composites was confirmed by using Fourier transform infrared (FTIR) spectroscopy. X-ray photoelectron spectroscopy (XPS) was carried out to analyze the chemical components of the composites [49]. The morphology of the composites was studied by using the scanning

electron microscopy (SEM) and X-ray diffractometer (XRD). The Brunauer–Emmett–Teller (BET) method was used to determine the specific surface areas and pore size distributions of the V_2O_5/f-CNT/PPy. The electrochemical properties of the V_2O_5/f-CNT/PPy composites based electrodes were evaluated through cyclic voltammetry (CV), the galvanostatic charge/discharge (GCD) method, and electrochemical impedance spectroscopy (EIS) in a three-electrode system using aqueous 1 M Na_2SO4 as the electrolyte. High capacitance value (1266 mF cm^{-2} at a current density of 1 mA cm^{-2}) and good cycling stability (with the retention of 83.0% of its initial capacitance after 10,000 charge-discharge cycles) were observed for the V_2O_5/f-CNT/PPy based electrode.

2. Results

2.1. Preparation of the V_2O_5/f-CNT/PPy Composite Film

The schematic illustration of the V_2O_5/f-CNT/PPy composite film fabrication process is shown in Figure 1a. Firstly, V_2O_5 powder is treated with H_2O_2 to obtain a hydrous V_2O_5 gel. The chemical reactions between V_2O_5 powder and H_2O_2 leading to the formation of V_2O_5 gel are given in Equations (1)–(5) [50]. The addition of V_2O_5 to H_2O_2 and DI water leads to an exothermic reaction and forms orange-colored diperoxovanadate anion $[VO(O_2)_2(OH_2)]^-$, as shown in Equation (1) [51]. The unstable peroxo species undergoes further decomposition in the presence of excess H_2O_2 giving rise to red monperoxovanadate cation $[VO(O_2)(OH_2)_3]^+$ (Equations (2) and (3)). Upon aging, no free hydrogen peroxide can be detected in the solution, and an aqueous solution of dioxovanadium cation $[VO_2]^+$ (Equation (4)) is obtained. The increase in the viscosity of the solution indicates the onset of hydrous vanadium oxide gel formation.

$$V_2O_5 + 4H_2O_2 \rightarrow 2[VO(O_2)_2(OH_2)]^- + 2H^+ + H_2O \quad (1)$$

$$V_2O_5 + 2H^+ + 2H_2O_2 + 3H_2O \rightarrow 2[VO(O_2)(OH_2)_3]^+ + O_2 \quad (2)$$

$$2[VO(O_2)_2(OH_2)]^- + 4H^+ + 2H_2O \rightarrow 2[VO(O_2)(OH_2)_3]^+ + O_2 \quad (3)$$

$$2[VO(O_2)(OH_2)_3]^+ \rightarrow 2[VO_2]^+ + O_2 + 6H_2O \quad (4)$$

$$[VO_2]^+ \rightarrow \text{gelation} \quad (5)$$

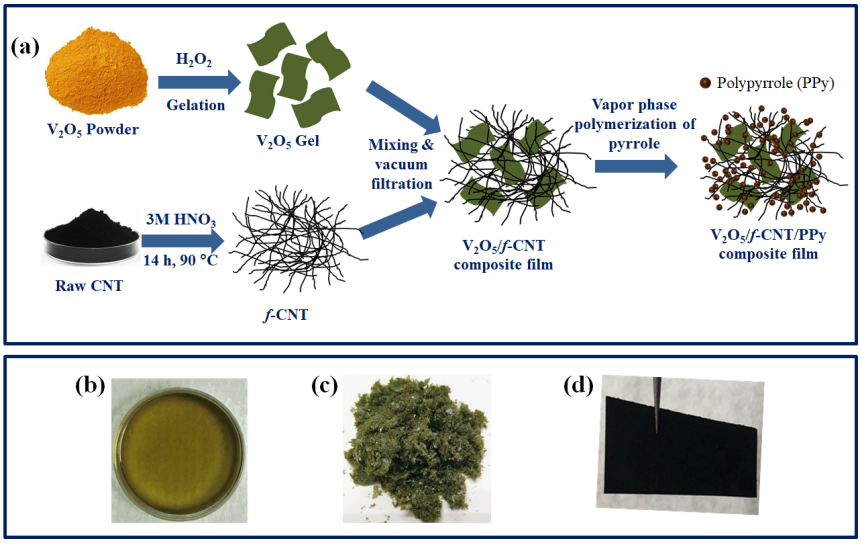

Figure 1. (**a**) schematic diagram of V_2O_5/f-CNT/PPy composite film fabrication process; photographs of (**b**) V_2O_5 gel, (**c**) freeze dried V_2O_5 gel, and (**d**) V_2O_5/f-CNT/PPy composite film.

The obtained hydrous vanadium oxide gel was mixed thoroughly with f-CNT dispersion and filtered off to formV_2O_5/f-CNT composite film. V_2O_5 and the intermediate

species such as HVO_4^{2-} and $H_2VO_4^{-}$, produced during the charge-discharge processes are readily soluble in aqueous electrolytes leading to poor cycling stability [25]. Therefore, the V_2O_5/*f*-CNT composite film was further coated with PPy by vapor phase polymerization to improve the conductivity and electrochemical stability of the composite film. The fabrication process of the V_2O_5/*f*-CNT/PPy composite film (Figure 1d) without any binder and additives is easy, low-cost, and scalable.

2.2. Characterization of the V_2O_5/*f*-CNT/PPy Composite Films

Figure 2 shows the FTIR spectra of *f*-CNT, V_2O_5 gel, V_2O_5/*f*-CNT, and V_2O_5/*f*-CNT/PPy. *f*-CNT spectra exhibited prominent characteristic peaks at 1697 and 1528 cm^{-1}, assigned to the stretching vibrations of C=O and COO–, respectively. The FTIR spectrum of V_2O_5 gel exhibited absorption bands at 1005 cm^{-1} corresponding to the stretching vibrations of V=O. The bands which appeared at 765 and 516 cm^{-1} are attributed to the asymmetric and symmetric stretching vibrations of V–O–V, respectively [52]. The peaks at 3438 and 1635 cm^{-1} correspond to the bending and stretching vibrations of H–O–H and O–H bonds due to the absorbed or bound water content in the material [46]. Major characteristic peaks of V_2O_5 gel and *f*-CNT are present in the FTIR spectrum of V_2O_5/*f*-CNT composite, indicating the successful integration of V_2O_5 and *f*-CNT in the composite. However, after the deposition of PPy, the intensity of absorption bands corresponding to V_2O_5 gel were reduced, which was corresponded to the coverage of PPy. In addition to the absorption peaks of V_2O_5 and *f*-CNT, the weak absorption peaks of PPy were observed ranged from 1250 to 1600 cm^{-1}.

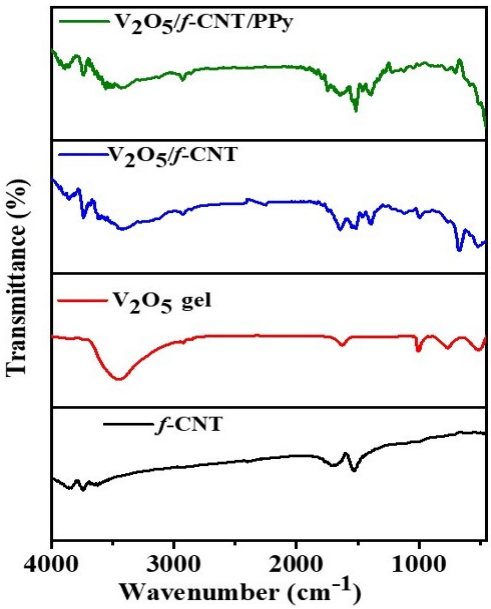

Figure 2. FTIR spectra of *f*-CNT, V_2O_5 gel, V_2O_5/*f*-CNT, and V_2O_5/*f*-CNT/PPy.

To study the crystallographic structure of the prepared materials, XRD analysis was conducted, and the data is shown in Figure 3. The pure V_2O_5 powder exhibited a highly crystalline orthorhombic phase [53]. On the other hand, the lack of sharp diffraction peaks in the XRD patterns of $V_2O_5.nH_2O$ gel indicates its poor crystallinity. The characteristics diffraction peaks of $V_2O_5.nH_2O$ gel appeared at 6.2°, 12.7°, 19.3°, and 25.8°. The intense peak at 6.2° corresponding to the (001) plane indicates the characteristic layered structure of $V_2O_5 \cdot nH_2O$ [50]. *f*-CNT exhibited a major diffraction peak at 25.5° which corresponds to the (002) lattice plane [54]. V_2O_5/*f*-CNT composite exhibited the characteristic peaks of both V_2O_5 and *f*-CNT, indicating their successful integration. The intensity of the diffraction peaks of V_2O_5 at 6.2° has been decreased after the deposition of PPy.

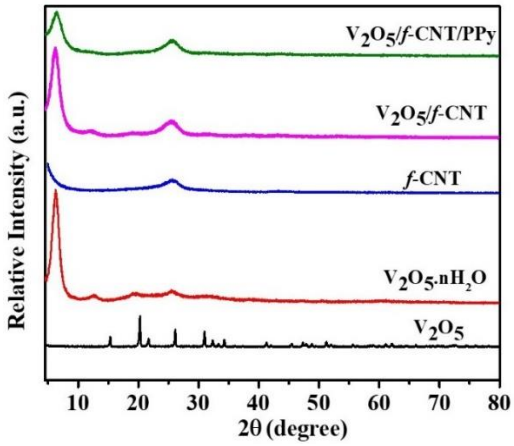

Figure 3. XRD patterns of V_2O_5 powder, $V_2O_5.nH_2O$ gel, *f*-CNT, V_2O_5/*f*-CNT, and V_2O_5/*f*-CNT/PPy.

TGA thermograms of V_2O_5 powder, V_2O_5 gel, V_2O_5/*f*-CNT, and V_2O_5/*f*-CNT/PPy composites are shown in Figure 4. V_2O_5 powder exhibited high thermal stability with a char yield of 98.4%, indicating its highly crystalline nature. The volatilization of adsorbed and interlayer water molecules causes a progressive weight loss in V_2O_5 gel at temperatures below 200 °C, showing its hygroscopic character. At temperatures above 200 °C, the removal of inter-layer water results in the conversion of the disordered layer phase to crystalline orthorhombic phase, resulting in high thermal stability for V_2O_5 gel at higher temperatures [55]. The improved thermal stability of V_2O_5/*f*-CNT composite compared with pure V_2O_5 gel is due to the presence of *f*-CNT. The weight loss in the V_2O_5/*f*-CNT composite at higher temperatures is mainly due to the removal of carboxyl groups from the surfaces of *f*-CNT. The continuous weight loss pattern observed for the V_2O_5/*f*-CNT/PPy composite can be ascribed to the degradation and decomposition of PPy in the composite.

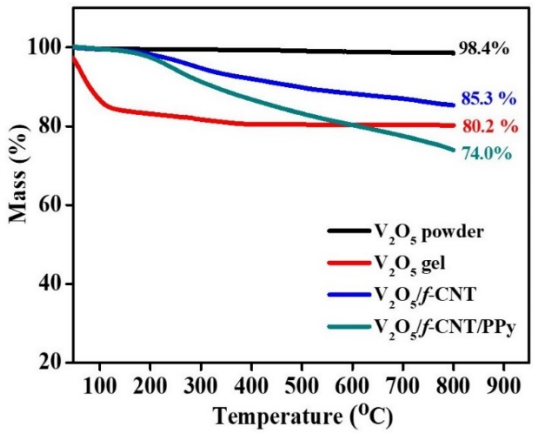

Figure 4. TGA thermograms of V_2O_5 powder, V_2O_5 gel, V_2O_5/*f*-CNT, and V_2O_5/*f*-CNT/PPy.

XPS measurement was used to analyze the surface composition and chemical structure of the V_2O_5/*f*-CNT/PPy composite. As shown in Figure 5a, the XPS survey spectrum exhibited four distinct peaks, indicating the presence of C, V, O, and N elements. The deconvoluted profile of V $2p_{3/2}$ core peak spectrum (Figure 5b) is composed of two components located at 517.2 eV and 515.8 eV, respectively, as shown in the fitting data. These two binding energy values indicate the existence of +5 and +4 oxidation states of vanadium in the V_2O_5/*f*-CNT/PPy composite with V^{5+} accounts for the majority of the spectra. Moreover, $V2p_{3/2}$ and $V2p_{1/2}$ have a binding energy difference of about 7.2 eV, confirming the predominance of +5 valence state of vanadium in V_2O_5/*f*-CNT/PPy composite [29,56]. The deconvoluted XPS spectrum for the O1s orbital exhibited three

bands at 532.2, 531.2, and 530.2 eV, corresponding to the O–C=O, V–OH, and V–O bonds, respectively (Figure 5c) [29,32]. A single peak appeared at 400 eV in the XPS spectrum for the N1s orbital (Figure 5d) was attributed to pyrrolic nitrogen [57].

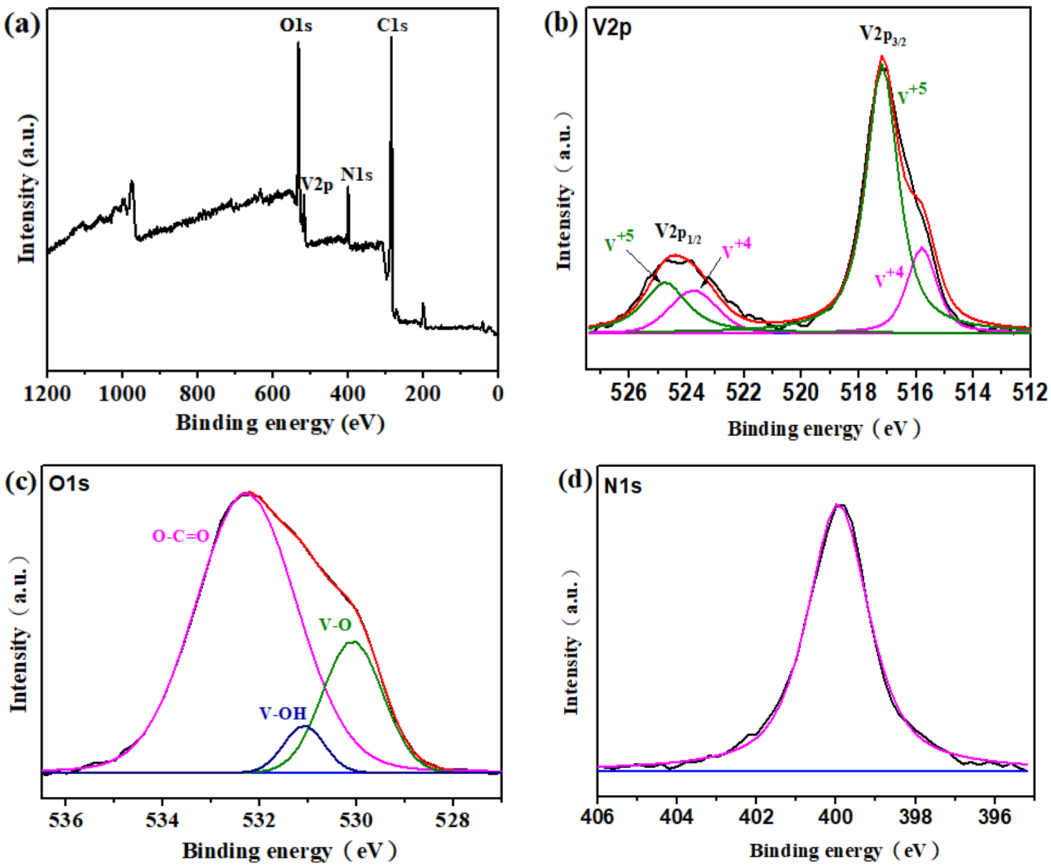

Figure 5. XPS (**a**) survey spectrum, scan of (**b**) V2p, (**c**) O1s, and (**d**) N1s of V_2O_5/f-CNT/PPy.

Figure 6 shows SEM images of f-CNT, V_2O_5 gel, V_2O_5/f-CNT, and $V2O_5$/f-CNT/PPy. In Figure 6a, the pure f-CNT film showed a densely packed network structure of f-CNT that was tightly interconnected. Sheet-like structures of V_2O_5 were visible in the SEM image of V_2O_5 gel (Figure 6b). Despite their high electronic conductivity and surface area, f-CNTs have a very low specific capacitance due to the electrical double-layer charge-storage process. As a result, pseudocapacitive materials with high theoretical capacitance are often combined with *f*-CNTs to improve the composites' total capacitance. Therefore, using a simple solution-based mixing technique, V_2O_5, a highly pseudocapacitive metal oxide, was integrated into the *f*-CNT network. V_2O_5 embedded in the *f*-CNT matrix can be seen in the SEM image of V_2O_5/*f*-CNT (Figure 6c). Figure 6d reveals the spherical PPy nanoparticles deposited on the V_2O_5/*f*-CNT/PPy composite after vapor phase polymerization. In Figure 7, the elemental mapping images of the V_2O_5/*f*-CNT/PPy reveal the homogeneous distribution of four elements C, V, O, and N in the composite. The C element comes from *f*-CNT, the V and O elements come from V_2O_5, and the N element comes from PPy.

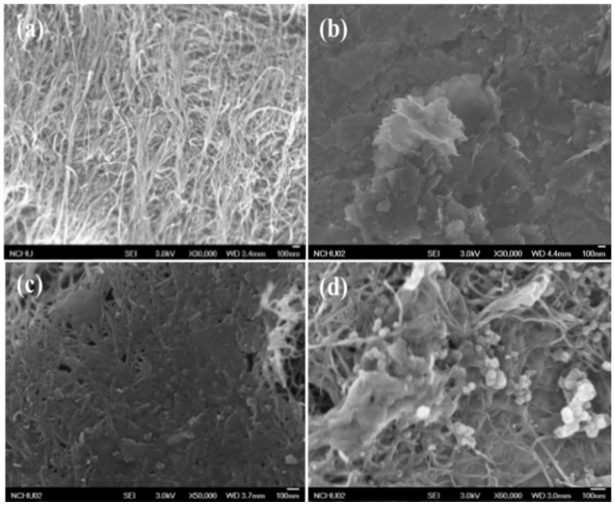

Figure 6. SEM images of (**a**) *f*-CNT, (**b**) V_2O_5 gel, (**c**) V_2O_5/*f*-CNT, and (**d**) V_2O_5/*f*-CNT/PPy.

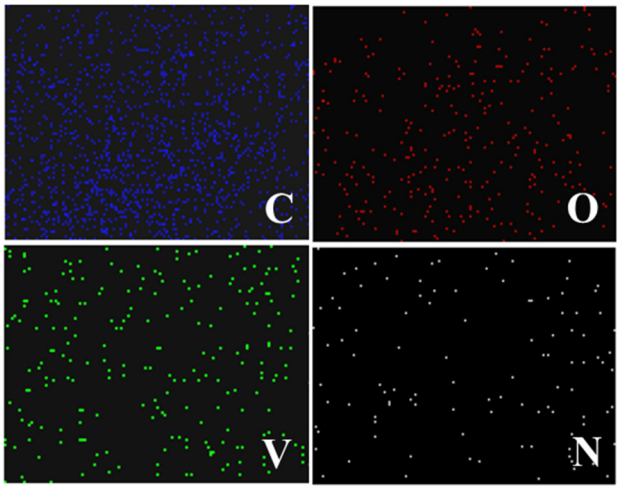

Figure 7. Elemental mapping images of V_2O_5/*f*-CNT/PPy.

Nitrogen adsorption/desorption test was used to analyze the porous structures of *f*-CNT, V_2O_5/*f*-CNT, and V_2O_5/*f*-CNT/PPy, as seen in Figure 8. Type IV isotherms with distinct hysteresis loops at moderate pressures revealed that all composite materials had porous structures dominated by mesopores [58]. The BET specific surface areas for *f*-CNT, V_2O_5/*f*-CNT, and V_2O_5/*f*-CNT/PPy were 270.66, 188.43, and 163.33 $m^2\ g^{-1}$, respectively. As compared to the *f*-CNT, lower specific surface areas was observed for the V_2O_5/*f*-CNT due to the coverage of V_2O_5 gel. Moreover, the surface area of the V_2O_5/*f*-CNT/PPy composite was slightly lower than the V_2O_5/*f*-CNT composite, which may be due to the PPy content partly blocking the pores in the composite. The average pore diameters estimated from the pore size distribution curves using the BJH technique for *f*-CNT, V_2O_5/*f*-CNT, and V_2O_5/*f*-CNT/PPy were 21.4, 19.7, and 12.2 nm, respectively. The distinctive hierarchical mesoporous architecture of V_2O_5/*f*-CNT/PPy composite with high specific surface areas allows for efficient use of the active materials by providing fast electrolyte diffusion pathways.

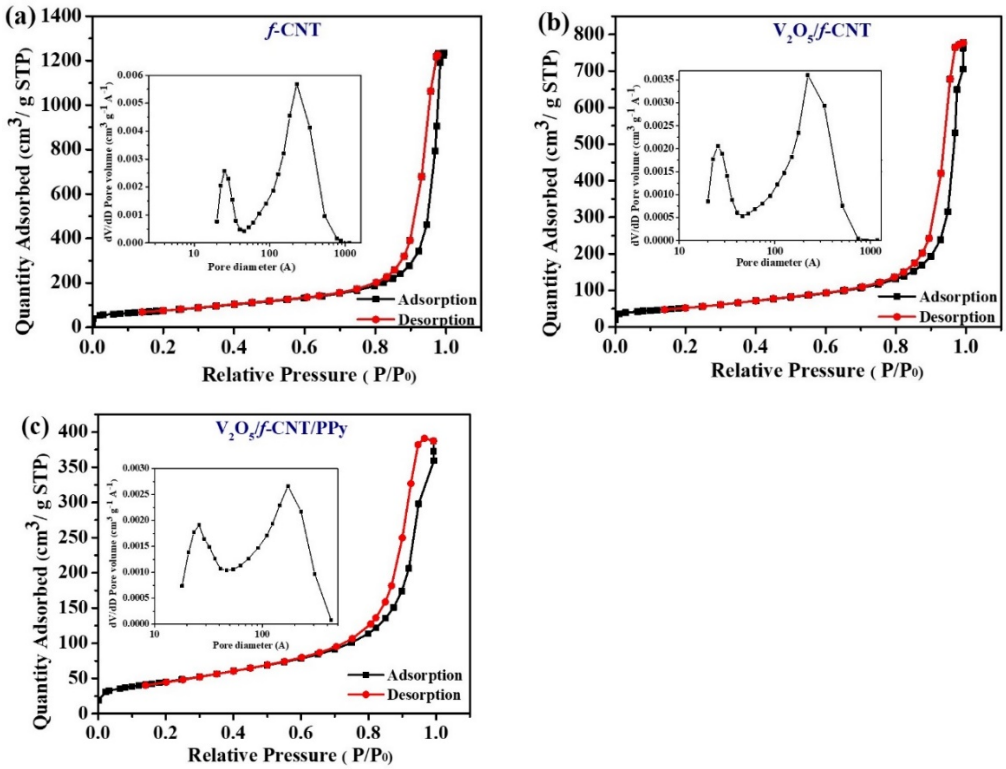

Figure 8. Nitrogen adsorption/desorption isotherms of (**a**) *f*-CNT, (**b**) V_2O_5/*f*-CNT, and (**c**) V_2O_5/*f*-CNT/PPy inset: pore size distribution curves.

2.3. Electrochemical Properties of the Freestanding Negative Electrodes

The CV plots measured at different scan rates of the *f*-CNT, V_2O_5/*f*-CNT, and V_2O_5/*f*-CNT/PPy composites in a three-electrode set-up are shown in Figure 9a–c. The CV curves of the *f*-CNT electrode were almost rectangular, indicating an ideal electrochemical double layer (EDL) capacitance. The quasi rectangular-shaped curves with high peak current response for V_2O_5/*f*-CNT and V_2O_5/*f*-CNT/PPy electrodes indicate that the capacitance was contributed by the pseudocapacitance of V_2O_5 and PPy in addition to the double-layer capacitance of *f*-CNTs. At all measured scan rates, the V_2O_5/*f*-CNT/PPy electrode had a much greater integrated area within the CV curve than the *f*-CNT and V_2O_5/*f*-CNT electrodes, demonstrating its superior performance. Figure 9d–f provides the GCD curves recorded at different current densities. The typical EDL capacitance of the *f*-CNT electrode was confirmed by GCD curves with symmetric triangular shapes at all current densities. The triangular-shaped GCD curves of V_2O_5/*f*-CNT, and V_2O_5/*f*-CNT/PPy composites with slight distortion and longer discharge times than the *f*-CNT electrode confirmed the pseudocapacitance contribution of V_2O_5 and PPy towards the total capacitance. In comparison to *f*-CNT electrode (490 mF cm^{-2}) and V_2O_5/*f*-CNT electrode (1061 mF cm^{-2}), V_2O_5/*f*-CNT/PPy electrode had the highest areal capacitance (1266 mF cm^{-2}). Moreover, a high volumetric capacitance of 126.6 F cm^{-3} was also achieved by the V_2O_5/*f*-CNT/PPy electrode. In addition to the partial contribution of pseudocapacitance from PPy, the electrochemical Na^+ insertion process occurring at V_2O_5/*f*-CNT and V_2O_5/*f*-CNT/PPy electrodes during the charge-discharge process can be expressed as $V_2O_5 + xNa^+ + xe^- \leftrightarrow Na_xV_2O_5$ [59,60]. The superior capacitance of the V_2O_5/*f*-CNT/PPy electrode can be ascribed to the improved conductivity as well as its highly porous architecture with large active surface area, which allowed a better use of the inner active redox sites in the electrode material. The electrochemical performance of the V_2O_5/*f*-CNT/PPy electrode was superior to those of many previously reported freestanding electrodes (see Table S1).

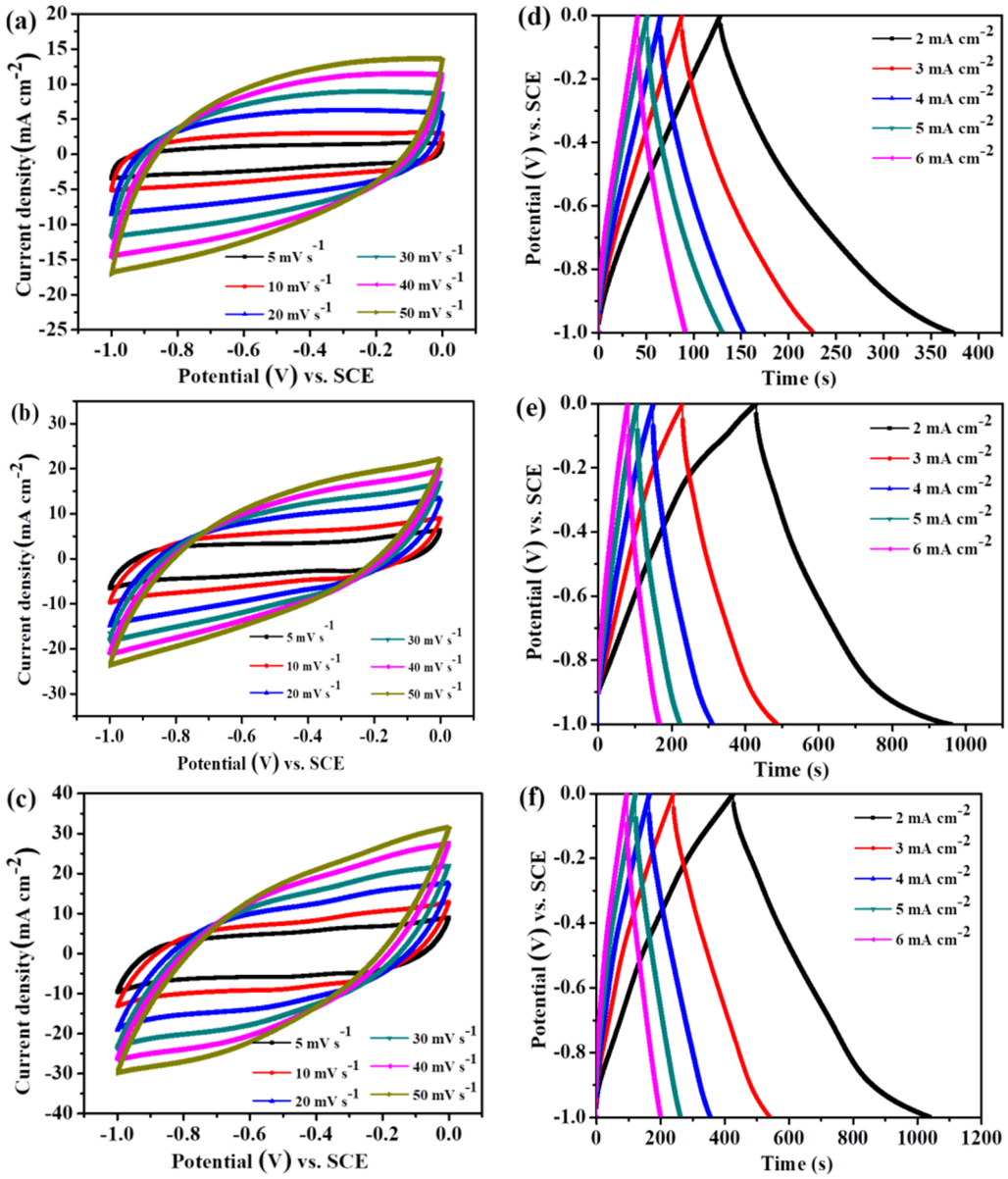

Figure 9. (**a**–**c**) CV curves at various scan rates and (**d**–**f**) GCD curves at various current densities of (**a**,**d**) the *f*-CNT, (**b**,**e**) the V_2O_5/*f*-CNT, and (**c**,**f**) the V_2O_5/*f*-CNT/PPy electrodes.

EIS was used to assess the resistance associated with charge storage at the electrode/electrolyte interface and to better understand the charge transfer mechanism in the electrode materials. The Nyquist plots of *f*-CNT, V_2O_5/*f*-CNT, and V_2O_5/*f*-CNT/PPy electrodes comprising a straight line in the low-frequency region and a semi-circle in the high-frequency region are shown in Figure 10a. By intersecting the semi-circle with the *X*-axis, the equivalent series resistance (R_s), which is the inner resistance of the electrode and electrolyte, is obtained, while the diameter of the semi-circle provides the charge transfer resistance (R_{ct}) at the electrode/electrolyte interface. The V_2O_5/*f*-CNT/PPy composite electrode exhibited good charge transfer properties due to the self-standing electrode structure that eliminates the need for an insulating binder for electrode fabrication. Moreover, the highly porous structures of the electrodes enable easy infiltration of electrolyte resulting in less ion diffusion resistance. The areal capacitances of the composite electrodes at various current densities are summarized in Figure 10b. The capacitances of all freestanding electrodes decreased as the current intensity rose. This reduction in the areal capacitance

is due to the reduced electrolyte ions accessibility to the inner active sites of the electrode materials, resulting in inadequate use of the V_2O_5 and PPy at higher current densities.

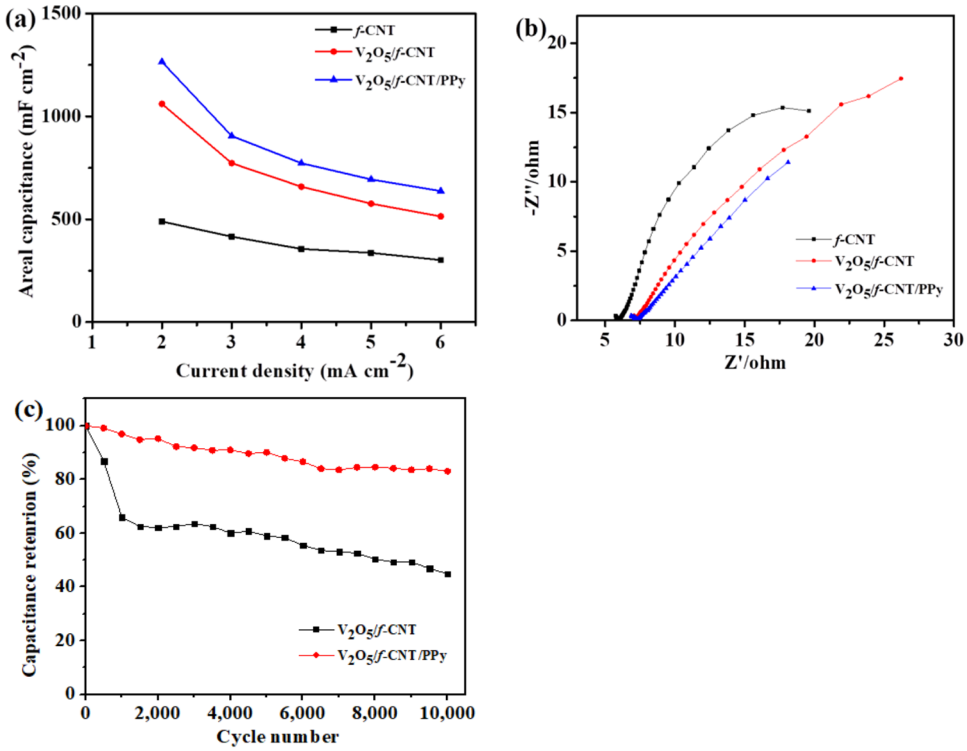

Figure 10. (**a**) EIS spectra, (**b**) areal capacitances vs. current density plot, and (**c**) cycle life test of V_2O_5/f-CNT and V_2O_5/f-CNT/PPy electrodes.

Since cycling stability is an important parameter for electrode materials, V_2O_5/f-CNT and V_2O_5/f-CNT/PPy electrodes were charged and discharged 10,000 times at a current density of 10 mA cm^{-2} to determine cycling performance. Figure 10c shows that the areal capacitance of both electrodes decreases with the increasing charge-discharge cycles. However, after 10,000 charge/discharge cycles, the V_2O_5/f-CNT/PPy electrode retained 83% of its original capacitance, whereas V_2O_5/f-CNT electrode could retain only 45% of its initial capacitance. The poor cycling performance of the V_2O_5/f-CNT electrode is due to the dissolution of V_2O_5, as indicated by the color change of the electrolyte solution during the charge-discharge process. The PPy protection layer prevents the dissolution of V_2O_5, resulting in improved stability for V_2O_5/f-CNT/PPy electrode.

3. Materials and Methods

3.1. Materials

CNTs were obtained from C-nano Technology (Beijing, China). Nitric Acid (HNO_3), urea [$CO(NH_2)_2$], and vanadium oxide (V_2O_5) powder were purchased from J.T.Baker Chemicals (Phillipsburg, NJ, USA). Sodium hydroxide (NaOH), iron(III) chloride hexahydrate ($FeCl_3.6H_2O$), and sodium sulfate (Na_2SO_4) were procured from Honeywell Fluka (Charlotte, NC, USA). Thiourea [$SC(NH_2)_2$], hydrogen peroxide (H_2O_2, 30% *w*/*w*), and sulfuric acid (H_2SO_4) were obtained from Showa Chemical Industry (Minato-ku, Tokyo, Japan). Acetic acid (CH_3COOH), pyrrole (C_4H_4NH), and sodium chlorite ($NaClO_2$) were purchased from Sigma–Aldrich (St. Louis, MO, USA). High-purity deionized water was used in all experimental processes.

3.2. Preparation of Vanadium Pentoxide Gel

First, 0.2 g of V_2O_5 powder was added into 20 mL of deionized water and stirred at 60 °C at high speed. Then, 2 mL of H_2O_2 was slowly dropped into the V_2O_5 suspension and continued stirring for 20 min until a red solution was obtained. After cooling the reaction mixture to room temperature, 20 mL of ethanol was added and allowed to age for 7 days to obtain a homogeneous green viscous gel.

3.3. Preparation of V_2O_5/f-CNTs Composite Film

To prepare the *f*-CNTs, CNTs were treated with 3 M nitric acid under reflux for 14 h at 90 °C, followed by 1 h ultrasonication. The dried *f*-CNTs (50 mg) were then ultrasonically dispersed in DI water. Then, 45 mg of *f*-CNTs were dispersed well in 45 mL of ethanol by ultrasonication for 1 h. Next, 5 mL (25 mg of V_2O_5) of V_2O_5 gel was then dropped slowly into the *f*-CNT dispersion at room temperature under magnetic stirring. After 1 h reaction, the reaction mixture was filtered by vacuum suction to form V_2O_5/f-CNTs composite film. The composite film was washed thoroughly with deionized water several times and dried in a vacuum oven at 60 °C for 12 h. The mass ratio of V_2O_5/f-CNTs was 36/64 (*w*/*w*).

3.4. Preparation of V_2O_5/f-CNT/PPy Composite Film

PPy was coated on V_2O_5/f-CNT composite film through a simple vapor phase polymerization method at room temperature. The V_2O_5/f-CNT composite film was first immersed in a 1 M aqueous $FeCl_3 \cdot 6H_2O$ solution for 10 min. After drying the composite film at room temperature, it was placed in a vacuum flask. Then, 2 mL of purified pyrrole monomer was placed in a Petri plate and allowed to evaporate inside the vacuum flask. The interaction of the pyrrole vapors with $FeCl_3 \cdot 6H_2O$ initiates the polymerization process to form a PPy layer on the composite film. The polymerization time was adjusted to 10 min to obtain the V_2O_5/f-CNT/PPy composite film. The as-prepared composite film was washed thoroughly with DI water and then dried in a vacuum oven at 60 °C for 12 h.

3.5. Characterizations

FTIR spectra of the samples were recorded using a PerkinElmer RX1 IR spectrophotometer (PerkinElmer, Taipei, Taiwan). Thermogravimetric analysis (TGA, PerkinElmer Pyris1, PerkinElmer, Taipei, Taiwan) was performed under an N_2 atmosphere at a heating rate of 10 °C min^{-1}. SEM (Jeol-JSM-7401F, Jeol, Tokyo, Japan) was used to observe the morphologies and microstructures of the prepared samples. The crystallographic structures of the prepared materials were analyzed using XRD (Bruker AXS, Bruker Taiwan Co. Ltd., Hsinchu, Taiwan, Cu Kα radiation). XPS (ESCALAB 250Xi, Thermo Fisher, Waltham, MA, USA) was used to examine the surface chemical components of the samples. Nitrogen adsorption/desorption isotherms of the composite samples were recorded using a surface area and porosity analyzer (ASAP 2010, Micromeritics, Merit Sci. Corp., Taipei, Taiwan). From the linear regions of the isotherms, the Brunauer–Emmett–Teller (BET) technique was applied to calculate the specific surface areas. The Barret–Joyner–Halenda (BJH) technique was used to determine pore size distributions from the desorption branches of the isotherms.

3.6. Electrochemical Measurements

CV, GCD, and EIS measurements were performed using a three-electrode system on an electrochemical work station (CH Instruments, Austin, TX, USA) to evaluate the electrochemical properties of the prepared composite materials. The reference electrode, counter electrode, and electrolyte were saturated calomel electrodes (SCE), platinum foil, and 1 M Na_2SO_4, respectively. As the working electrode, a piece of composite film (1.0 by 1.0 cm) was utilized directly. CV and GCD analyses were performed in the voltage range from 0 to −1 V at various scan rates and applied current densities, respectively. The

areal capacitances (C_A, F cm^{-2}) of freestanding negative electrodes were calculated from the GCD curves using Equation (6) [7]:

$$C_A = \frac{I\Delta t}{A_s \Delta V} \tag{6}$$

where I is the discharge current (A), Δt is the discharge time (s), A_s is the area of the freestanding electrode (cm^2), and ΔV is the potential window (V) excluding the IR drop.

The volumetric capacitance (C_v, F cm^{-3}) was calculated using the Equation (7):

$$C_v = \frac{C_A}{d} \tag{7}$$

where d is the thickness (cm) of the single electrode.

4. Conclusions

A simple, straightforward, and efficient approach was developed for the production of V_2O_5/*f*-CNT/PPy composite electrode. Firstly, a hydrous V_2O_5 gel was prepared by treating V_2O_5 powder with H_2O_2. The as-prepared V_2O_5 gel was then dispersed uniformly in the *f*-CNT matrix to obtain V_2O_5/*f*-CNT composite electrode. V_2O_5/CNT was then coated with a PPy layer by the vapor-phase polymerization method. The PPy coating on the V_2O_5/CNT prevented the dissolution of V_2O_5 and thus improved the capacitance and cycle life stability for V_2O_5/CNT/PPy composite electrode. The V_2O_5/*f*-CNT/PPy negative electrode exhibited outstanding electrochemical properties due to the synergistic effects of highly conductive *f*-CNTs and pseudocapacitive V_2O_5. The V_2O_5/*f*-CNT/PPy electrode exhibited a high areal capacitance of 1266 mF cm^{-2} and excellent cycling stability with 83% capacitance retention after 10,000 charge-discharge cycles.

Supplementary Materials: The following are available online at https://www.mdpi.com/article/10.3390/catal11080980/s1.

Author Contributions: Conceptualization R.-H.L. and J.P.J.; Methodology M.-Z.C., Y.-C.T., E.-C.C., and Y.-C.L.; Validation, R.-H.L.; Investigation, R.-H.L., M.-Z.C., and Y.-C.T.; Resources, R.-H.L.; Writing—Original Draft Preparation, J.P.J.; Writing—Review & Editing, R.-H.L., J.P.J., C.-C.K., and T.-C.C.; Supervision, R.-H.L.; Project Administration, R.-H.L.; Funding Acquisition, R.-H.L. All authors have read and agreed to the published version of the manuscript.

Funding: This research was funded by the Ministry of Science and Technology (MOST) of Taiwan (grant no. MOST 109-2221-E-005 -070 -MY3.

Data Availability Statement: Data is contained within the article.

Acknowledgments: The authors are grateful for the financial support provided by the MOST of Taiwan.

Conflicts of Interest: The authors declare no conflict of interest.

References

1. Wu, Z.; Li, L.; Yan, J.M.; Zhang, X.B. Materials design and system construction for conventional and new-concept supercapacitors. *Adv. Sci.* **2017**, *4*, 1600382. [CrossRef]
2. Cao, A.; Chen, Z.; Wang, Y.; Zhang, J.; Wang, Y.; Li, T.; Han, Y. Redox-active doped polypyrrole microspheres induced by phosphomolybdic acid as supercapacitor electrode materials. *Synth. Met.* **2019**, *252*, 135–141. [CrossRef]
3. Zhang, X.; Jiang, C.; Liang, J.; Wu, W. Electrode materials and device architecture strategies for flexible supercapacitors in wearable energy storage. *J. Mater. Chem. A* **2021**, *9*, 8099–8128. [CrossRef]
4. Jyothibasu, J.P.; Lee, R.H. Facile, scalable, eco-friendly fabrication of high-performance flexible all-solid-state supercapacitors. *Polymers* **2018**, *10*, 1247. [CrossRef]
5. Xu, J.; Zhu, L.; Bai, Z.; Liang, G.; Liu, L.; Fang, D.; Xu, W. Conductive polypyrrole–bacterial cellulose nanocomposite membranes as flexible supercapacitor electrode. *Org. Electron.* **2013**, *14*, 3331–3338. [CrossRef]
6. Zhao, J.; Wu, J.; Li, B.; Du, W.; Huang, Q.; Zheng, M.; Xue, H.; Pang, H. Facile synthesis of polypyrrole nanowires for high-performance supercapacitor electrode materials. *Prog. Nat. Sci. Mater. Int.* **2016**, *26*, 237–242. [CrossRef]

7. Jyothibasu, J.P.; Wang, R.-H.; Ong, K.; Ong, J.H.L.; Lee, R.-H. Cellulose/carbon nanotube/MnO_2 composite electrodes with high mass loadings for symmetric supercapacitors. *Cellulose* **2021**, *28*, 3549–3567. [CrossRef]
8. Jyothibasu, J.P.; Kuo, D.W.; Lee, R.H. Flexible and freestanding electrodes based on polypyrrole/carbon nanotube/cellulose composites for supercapacitor application. *Cellulose* **2019**, *26*, 4495–4513. [CrossRef]
9. Forouzandeh, P.; Vignesh, K.; Pillai, S. Electrode materials for supercapacitors: A review of recent advances. *Catalysts* **2020**, *10*, 969. [CrossRef]
10. An, H.; Wang, Y.; Wang, X.; Zheng, L.; Wang, X.; Yi, L.; Bai, L.; Zhang, X. Polypyrrole/carbon aerogel composite materials for supercapacitor. *J. Power Sources* **2010**, *195*, 6964–6969. [CrossRef]
11. Li, Z.; Cai, J.; Cizek, P.; Niu, H.; Du, Y.; Lin, T. A self-supported, flexible, binder-free pseudo-supercapacitor electrode material with high capacitance and cycling stability from hollow, capsular polypyrrole fibers. *J. Mater. Chem. A* **2015**, *3*, 16162–16167. [CrossRef]
12. Song, Y.; Liu, T.Y.; Xu, X.X.; Feng, D.Y.; Li, Y.; Liu, X.X. Pushing the cycling stability limit of polypyrrole for supercapacitors. *Adv. Funct. Mater.* **2015**, *25*, 4626–4632. [CrossRef]
13. Choudhary, N.; Li, C.; Moore, J.; Nagaiah, N.; Zhai, L.; Jung, Y.; Thomas, J. Asymmetric supercapacitor electrodes and devices. *Adv. Mater.* **2017**, *29*, 1605336. [CrossRef] [PubMed]
14. Gu, P.; Liu, W.; Hou, Q.; Ni, Y. Lignocellulose-derived hydrogel/aerogel-based flexible quasi-solid-state supercapacitors with high-performance: A review. *J. Mater. Chem. A* **2021**, *9*, 14233–14264. [CrossRef]
15. Khan, J.H.; Lin, J.; Young, C.; Matsagar, B.M.; Wu, K.C.W.; Dhepe, P.L.; Islam, M.T.; Rahman, M.; Shrestha, L.K.; Alshehri, S.M.; et al. High surface area nanoporous carbon derived from high quality jute from bangladesh. *Mater. Chem. Phys.* **2018**, *216*, 491–495. [CrossRef]
16. Khan, J.H.; Marpaung, F.; Young, C.; Lin, J.; Islam, M.T.; Alsheri, S.M.; Ahamad, T.; Alhokbany, N.; Ariga, K.; Shrestha, L.K.; et al. Jute-derived microporous/mesoporous carbon with ultra-high surface area using a chemical activation process. *Microporous Mesoporous Mater.* **2019**, *274*, 251–256. [CrossRef]
17. El-Mahdy, A.F.; Young, C.; Kim, J.; You, J.; Yamauchi, Y.; Kuo, S.W. Hollow microspherical and microtubular [3+3] carbazole-based covalent organic frameworks and their gas and energy storage applications. *ACS Appl. Mater. Interfaces* **2019**, *11*, 9343–9354. [CrossRef]
18. Zhang, Y.; Yuan, X.; Lu, W.; Yan, Y.; Zhu, J.; Chou, T.-W. MnO_2 based sandwich structure electrode for supercapacitor with large voltage window and high mass loading. *Chem. Eng. J.* **2019**, *368*, 525–532. [CrossRef]
19. Lao, Z.J.; Konstantinov, K.; Tournaire, Y.; Ng, S.H.; Wang, G.X.; Liu, H.K. Synthesis of vanadium pentoxide powders with enhanced surface-area for electrochemical capacitors. *J. Power Sources* **2006**, *162*, 1451–1454. [CrossRef]
20. Tian, Y.; Hu, X.; Wang, Y.; Li, C.; Wu, X. Fe_2O_3 nanoparticles decorated on graphene-carbon nanotubes conductive networks for boosting the energy density of all-solid-state asymmetric supercapacitor. *ACS Sustain. Chem. Eng.* **2019**, *7*, 9211–9219. [CrossRef]
21. Meher, S.K.; Rao, G.R. Ultralayered Co_3O_4 for high-performance supercapacitor applications. *J. Phys. Chem. C* **2011**, *115*, 15646–15654. [CrossRef]
22. Reddy, R.N.; Reddy, R.G. Synthesis and electrochemical characterization of amorphous MnO_2 electrochemical capacitor electrode material. *J. Power Sources* **2004**, *132*, 315–320. [CrossRef]
23. Yao, D.; Ouyang, Y.; Jiao, X.; Ye, H.; Lei, W.; Xia, X.; Lu, L.; Hao, Q. Hierarchical NiO@$NiCo_2O_4$ core–shell nanosheet arrays on Ni foam for high-performance electrochemical supercapacitors. *Ind. Eng. Chem. Res.* **2018**, *57*, 6246–6256. [CrossRef]
24. Wang, Y.; Cao, G. Synthesis and enhanced intercalation properties of nanostructured vanadium oxides. *Chem. Mater.* **2006**, *18*, 2787–2804. [CrossRef]
25. Ghosh, M.; Vijayakumar, V.; Soni, R.; Kurungot, S. A rationally designed self-standing V_2O_5 electrode for high voltage non-aqueous all-solid-state symmetric (2.0 V) and asymmetric (2.8 V) supercapacitors. *Nanoscale* **2018**, *10*, 8741–8751. [CrossRef]
26. Chernova, N.A.; Roppolo, M.; Dillon, A.C.; Whittingham, M.S. Layered vanadium and molybdenum oxides: Batteries and electrochromics. *J. Mater. Chem.* **2009**, *19*, 2526–2552. [CrossRef]
27. Velmurugan, R.; Premkumar, J.; Pitchai, R.; Ulaganathan, M.; Subramanian, B. Robust, flexible, and binder Free highly Crystalline V_2O_5 thin film electrodes and their superior supercapacitor performances. *ACS Sustain. Chem. Eng.* **2019**, *7*, 13115–13126. [CrossRef]
28. Zhang, H.; Han, X.; Gan, R.; Guo, Z.; Ni, Y.; Zhang, L. A facile biotemplate-assisted synthesis of mesoporous V_2O_5 microtubules for high performance asymmetric supercapacitors. *Appl. Surf. Sci.* **2020**, *511*, 145527. [CrossRef]
29. Panigrahi, K.; Howli, P.; Chattopadhyay, K.K. 3D network of V_2O_5 for flexible symmetric supercapacitor. *Electrochim. Acta* **2020**, *337*, 135701. [CrossRef]
30. Kim, I.-H.; Kim, J.-H.; Cho, B.-W.; Lee, Y.-H.; Kim, K.-B. Synthesis and electrochemical characterization of vanadium oxide on carbon nanotube film substrate for pseudocapacitor applications. *J. Electrochem. Soc.* **2006**, *153*, A989. [CrossRef]
31. Perera, S.D.; Patel, B.; Nijem, N.; Roodenko, K.; Seitz, O.; Ferraris, J.P.; Chabal, Y.J.; Balkus, K.J., Jr. Vanadium oxide nanowire–carbon nanotube binder-free flexible electrodes for supercapacitors. *Adv. Energy Mater.* **2011**, *1*, 936–945. [CrossRef]
32. Mtz-Enriquez, A.I.; Gomez-Solis, C.; Oliva, A.I.; Zakhidov, A.; Martinez, P.M.; Garcia, C.R.; Herrera-Ramirez, A.; Oliva, J. Enhancing the voltage and discharge times of graphene supercapacitors depositing a CNT/V_2O_5 layer on their electrodes. *Mater. Chem. Phys.* **2020**, *244*, 122698. [CrossRef]

33. Korkmaz, S.; Tezel, F.M.; Kariper, İ.A. Synthesis and characterization of GO/V_2O_5 thin film supercapacitor. *Synth. Met.* **2018**, *242*, 37–48. [CrossRef]
34. Zheng, P.; Lv, X.; Shi, S.; Liu, Y.; Yang, L.; Ge, D. High-efficiency supercapacitors based on V_2O_5/rGONR network from hierarchical nanoribbon assemblies. *J. Alloys Compd.* **2019**, *792*, 468–473. [CrossRef]
35. Bonso, J.S.; Rahy, A.; Perera, S.D.; Nour, N.; Seitz, O.; Chabal, Y.J.; Balkus, K.J., Jr.; Ferraris, J.P.; Yang, D.J. Exfoliated graphite nanoplatelets–V_2O_5 nanotube composite electrodes for supercapacitors. *J. Power Sources* **2012**, *203*, 227–232. [CrossRef]
36. Choudhury, A.; Bonso, J.S.; Wunch, M.; Yang, K.S.; Ferraris, J.P.; Yang, D.J. In-situ synthesis of vanadium pentoxide nanofibre/exfoliated graphene nanohybrid and its supercapacitor applications. *J. Power Sources* **2015**, *287*, 283–290. [CrossRef]
37. Lee, S.-M.; Park, Y.-J.; Lam, D.V.; Kim, J.-H.; Lee, K. Effects of annealing on electrochemical performance in graphene/V_2O_5 supercapacitor. *Appl. Surf. Sci.* **2020**, *512*, 145626. [CrossRef]
38. Liu, H.; Zhu, W.; Long, D.; Zhu, J.; Pezzotti, G. Porous V_2O_5 nanorods/reduced graphene oxide composites for high performance symmetric supercapacitors. *Appl. Surf. Sci.* **2019**, *478*, 383–392. [CrossRef]
39. Sathiya, M.; Prakash, A.S.; Ramesha, K.; Tarascon, J.M.; Shukla, A.K. V_2O_5-anchored carbon nanotubes for enhanced electrochemical energy storage. *J. Am. Chem. Soc.* **2011**, *133*, 16291–16299. [CrossRef] [PubMed]
40. Pande, S.A.; Pandit, B.; Sankapal, B.R. Vanadium oxide anchored MWCNTs nanostructure for superior symmetric electrochemical supercapacitors. *Mater. Des.* **2019**, *182*, 107972. [CrossRef]
41. Chen, Z.; Augustyn, V.; Wen, J.; Zhang, Y.; Shen, M.; Dunn, B.; Lu, Y. High-Performance supercapacitors based on intertwined CNT/V_2O_5 nanowire nanocomposites. *Adv. Mater.* **2011**, *23*, 791–795. [CrossRef]
42. Jiang, H.; Cai, X.; Qian, Y.; Zhang, C.; Zhou, L.; Liu, W.; Li, B.; Lai, L.; Huang, W. V_2O_5 embedded in vertically aligned carbon nanotube arrays as free-standing electrodes for flexible supercapacitors. *J. Mater. Chem. A* **2017**, *5*, 23727–23736. [CrossRef]
43. Guo, C.X.; Yilmaz, G.; Chen, S.; Chen, S.; Lu, X. Hierarchical nanocomposite composed of layered V_2O_5/PEDOT/MnO_2 nanosheets for high-performance asymmetric supercapacitors. *Nano Energy* **2015**, *12*, 76–87. [CrossRef]
44. Qian, T.; Xu, N.; Zhou, J.; Yang, T.; Liu, X.; Shen, X.; Liang, J.; Yan, C. Interconnected three-dimensional V_2O_5/polypyrrole network nanostructures for high performance solid-state supercapacitors. *J. Mater. Chem. A* **2015**, *3*, 488–493. [CrossRef]
45. Huguenin, F.; Ferreira, M.; Zucolotto, V.; Nart, F.C.; Torresi, R.M.; Oliveira, O.N. Molecular-level manipulation of V_2O_5/polyaniline layer-by-layer films to control electrochromogenic and electrochemical properties. *Chem. Mater.* **2004**, *16*, 2293–2299. [CrossRef]
46. Bi, W.; Wu, Y.; Liu, C.; Wang, J.; Du, Y.; Gao, G.; Wu, G.; Cao, G. Gradient oxygen vacancies in V_2O_5/PEDOT nanocables for high-performance supercapacitors. *ACS Appl. Energy Mater.* **2019**, *2*, 668–677. [CrossRef]
47. Bi, W.; Jahrman, E.; Seidler, G.; Wang, J.; Gao, G.; Wu, G.; Atif, M.; AlSalhi, M.; Cao, G. Tailoring energy and power density through controlling the concentration of oxygen vacancies in V_2O_5/PEDOT Nanocable-Based Supercapacitors. *ACS Appl. Mater. Interfaces* **2019**, *11*, 16647–16655. [CrossRef]
48. Bi, W.; Huang, J.; Wang, M.; Jahrman, E.P.; Seidler, G.T.; Wang, J.; Wu, Y.; Gao, G.; Wu, G.; Cao, G. V_2O_5–Conductive polymer nanocables with built-in local electric field derived from interfacial oxygen vacancies for high energy density supercapacitors. *J. Mater. Chem. A* **2019**, *7*, 17966–17973. [CrossRef]
49. Kónya, Z.; Vesselényi, I.; Kiss, J.; Farkas, A.; Oszkó, A.; Kiricsi, I. XPS study of multiwall carbon nanotube synthesis on Ni-, V-, and Ni, V-ZSM-5 catalysts. *Appl. Catal. A Gen.* **2004**, *260*, 55–61. [CrossRef]
50. Liu, Y.; Clark, M.; Zhang, Q.; Yu, D.; Liu, D.; Liu, J.; Cao, G. V_2O_5 nano-electrodes with high power and energy densities for thin film Li-ion batteries. *Adv. Energy Mater.* **2011**, *1*, 194–202. [CrossRef]
51. Alonso, B.; Livage, J. Synthesis of vanadium oxide gels from peroxovanadic acid solutions: A ^{51}V NMR study. *J. Solid State Chem.* **1999**, *148*, 16–19. [CrossRef]
52. Roy, A.; Ray, A.; Sadhukhan, P.; Saha, S.; Das, S. Morphological behaviour, electronic bond formation and electrochemical performance study of V_2O_5-polyaniline composite and its application in asymmetric supercapacitor. *Mater. Res. Bull.* **2018**, *107*, 379–390. [CrossRef]
53. Mjejri, I.; Gaudon, M.; Song, G.; Labrugère, C.; Rougier, A. Crystallized V_2O_5 as oxidized phase for unexpected multicolor electrochromism in V_2O_3 thick film. *ACS Appl. Energy Mater.* **2018**, *1*, 2721–2729. [CrossRef]
54. Jyothibasu, J.P.; Lee, R.H. Green synthesis of polypyrrole tubes using curcumin template for excellent electrochemical performance in supercapacitors. *J. Mater. Chem. A* **2020**, *8*, 3186–3202. [CrossRef]
55. Liu, Q.; Li, Z.F.; Liu, Y.; Zhang, H.; Ren, Y.; Sun, C.J.; Lu, W.; Zhou, Y.; Stanciu, L.; Stach, E.A.; et al. Graphene-modified nanostructured vanadium pentoxide hybrids with extraordinary electrochemical performance for Li-ion batteries. *Nat. Commun.* **2015**, *6*, 6127. [CrossRef]
56. You, M.; Zhang, W.; Yan, X.; Jiang, H.; Miao, J.; Li, Y.; Zhou, W.; Zhu, Y.; Cheng, X. V_2O_5 nanosheets assembled on 3D carbon fiber felt as a free-standing electrode for flexible asymmetric supercapacitor with remarkable energy density. *Ceram. Int.* **2021**, *47*, 3337–3345. [CrossRef]
57. Hou, Z.Q.; Wang, Z.Y.; Yang, L.X.; Yang, Z.G. Nitrogen-doped reduced graphene oxide intertwined with V_2O_3 nanoflakes as self-supported electrodes for flexible all-solid-state supercapacitors. *RSC Adv.* **2017**, *7*, 25732–25739. [CrossRef]
58. Jyothibasu, J.P.; Chen, M.Z.; Lee, R.H. Polypyrrole/carbon nanotube freestanding electrode with excellent electrochemical properties for high-performance all-solid-state supercapacitors. *ACS Omega* **2020**, *5*, 6441–6451. [CrossRef]

59. Saravanakumar, B.; Purushothaman, K.K.; Muralidharan, G. Interconnected V_2O_5 nanoporous network for high-performance supercapacitors. *ACS Appl. Mater. Interfaces* **2012**, *4*, 4484–4490. [CrossRef]
60. Wang, X.; Zuo, C.; Jia, L.; Liu, Q.; Guo, X.; Jing, X.; Wang, J. Synthesis of sandwich-like vanadium pentoxide/carbon nanotubes composites for high performance supercapacitor electrodes. *J. Alloys Compd.* **2017**, *708*, 134–140. [CrossRef]